

Visiting Scientist mission report

Document NWPSAF-KN-VS-008

Version 1.0

3 February 2012

Second-order structure function analysis of scatterometer winds over the Tropical Pacific: Part 1. Spectra and Structure Functions

Gregory P. King, Jur Vogelzang and Ad Stoffelen

 	Second-order structure function analysis of scatterometer winds over the Tropical Pacific: Part 1. Spectra and Structure Functions	Doc ID : NWPSAF-KN-VS-008 Version : 1.0 Date : 3 February 2012
--	---	--

This documentation was developed within the context of the EUMETSAT Satellite Application Facility on Numerical Weather Prediction (NWP SAF), under the Cooperation Agreement dated 1 December, 2006, between EUMETSAT and the Met Office, UK. The partners in the NWP SAF are the Met Office, ECMWF, KNMI and Météo France.

Copyright 2012, EUMETSAT, All Rights Reserved.

Change record			
Version	Date	Author / changed by	Remarks
1.0	3.2.12	G.P.King, J.Vogelzang and A.Stoffelen	Version for distribution.

Second-order structure function analysis of scatterometer winds over the Tropical Pacific: Part 1. Spectra and Structure Functions

Gregory P. King¹, Jur Vogelzang², and Ad Stoffelen²

¹*Centro de Geofisica - IDL, Campo Grande, C8, University of Lisbon, 1749-016
Lisbon, Portugal*

²*KNMI Royal Netherlands Meteorological Institute, Postbus 201, 3730 AE De
Bilt, The Netherlands*

Doc ID: NWPSAF-KN-VS-008

February 3, 2012

Abstract

A comparison of wind products derived from measurements by the SeaWinds and ASCAT scatterometers is carried out using second-order statistics calculated from wind spectra and Kolmogorov second-order structure functions. The comparison is made for equatorial winds in the Pacific during January 2009 between latitudes 10°S and 10°N. This region is subdivided into three longitudinal zones: (i) West Pacific (140°-180°E), (ii) Central Pacific (180°-220°E) and (iii) East Pacific (220°-260°E). Due to rain contamination of SeaWinds-winds and the sample length requirement for calculating spectra, only ASCAT winds could be used to compare spectra and structure functions. Results obtained by both methods were in good agreement, and the practical advantages of calculating structure functions were demonstrated.

Structure functions are tolerant of missing data, which allowed comparison of SeaWinds-winds and ASCAT-winds in both rainy and dry regions of the equatorial Pacific. The small r structure function shape was found to be wind-product-dependent. Slopes calculated in the meso-beta range demonstrated the effects of noise level and spatial filtering. A number of recommendations for future work are made.

Contents

1	Introduction	4
2	Statistical tools	5
2.1	Structure functions, covariance functions and spectra.	5
2.1.1	Physical interpretations	6
2.2	Connecting with observations	6
2.2.1	Closer to reality: sampled data	7
3	Scatterometer Data	8
4	Methodology	10
5	Results	12
5.1	Tropical Pacific rain	12
5.2	Spectra	12
5.3	Structure functions	13
6	Conclusions and Recommendations	15
6.1	Recommendations for further work	16

List of Figures

- 1 Study area in the Pacific — between latitudes 10°S and 10°N, divided into three longitudinal zones
- 2 Latitude-time plots of the rain rate (mm/hr) for the period November 2008 – October 2009. The r
- 3 Number of spectra averaged to produce Fig. 4. The small number of SeaWinds samples is due to r
- 4 Wind spectra calculated using along-swath samples between latitudes 10°S and 10°N: Along-swath
- 5 The spectral ratio ψ_{22a}/ψ_{11a} vs r for ASCAT-12.5 (black) and ASCAT-25 (blue). 24
- 6 Representation error estimated from the spectra using Eq. (31): RE_{11a}^{ψ} (dashed) and RE_{22a}^{ψ} (solid)
- 7 The number of pairs as a function of r used to calculate the structure functions shown in Fig. 8.
- 8 Second-order structure functions for latitudes 10°S–10°N. Also shown are the structure functions fo
- 9 Structure function ratios D_{22a}/D_{11a} vs r . Compare with Fig. 5 and note the large difference in the
- 10 Representation error estimated from the structure functions shown in Fig. 8. Dashed lines are RE_{11a}^D
- 11 Equatorial winds superimposed on sea surface temperatures. Winds and sea surface temperatures a

List of Tables

- 1 Wind products compared in this work. u_{rms} and v_{rms} taken from Vogelzang et al. [2011] 20
- 2 Spectral slopes estimated from linear fits in log-log space in the meso-beta range of scales (indicate
- 3 Rankings of structure function meso-beta range slopes (γ_{11a} , γ_{22a}) estimated from linear fits to (D_{11a}
- 4 Rankings of the structure function representation error. Top-to-bottom are furthest-to-closest to

1 Introduction

The global near-surface ocean wind field measured by satellite scatterometers is important for marine weather forecasting, validating numerical weather prediction (NWP) models and ocean modelling [Bourassa et al., 2010]. It is also important for testing ideas about the nature of atmospheric turbulence.

Scatterometers measure the radar backscatter cross section of the ocean surface. A Geophysical Model Function (GMF) relates the radar cross section to wind speed and direction [Stoffelen and Portabella, 2006]. In order to characterize noise properties and true spatial resolution, wind retrievals are validated and calibrated using buoy and NWP model winds [Vogelzang et al., 2011]. Scatterometers resolve the meso-beta (~ 20 -200 km) and meso-alpha (~ 200 -2000 km) subranges defined by Orlandi [1975]. Meso-beta range weather phenomena include convective clusters and precipitation bands, while meso-alpha phenomena include squall lines, mesoscale convective systems, tropical cyclones and extratropical cyclones.

Spectral methods have been used extensively for assessing the quality of scatterometer wind products, in particular for characterizing noise properties and true spatial resolution [Vogelzang et al., 2011]. The objective of this paper is to demonstrate the use of a different, but related tool which has some advantages over spectra: correlation functions of velocity differences. Hereafter, we follow the convention in the turbulence literature and refer to these correlation functions as *structure functions*.

Velocity structure functions are in Fourier duality with wind spectra [c.f., Babiano et al., 1985], and therefore contain equivalent information. In practice, however, it is important to demonstrate equivalence. This will be done for the scatterometer winds considered in this paper.

Structure functions are calculated in the spatial domain. They are much more tolerant of missing data and therefore make better use of the available information than do spectra. Furthermore, unlike spectral methods, there is no requirement on sample length. This means that structure functions can be applied to investigate small regions with particular turbulence characteristics. This will be demonstrated in the sequel to this paper.

Structure functions have other advantages: (i) because they give a real-space description of the energy distribution, relating them to features in the wind field is more direct; and (ii) there is no need to detrend the data.

Wind spectra and structure functions are calculated for wind products derived from measurements by the SeaWinds and ASCAT scatterometers (Table 1). The ASCAT and SeaWinds-KNMI products were developed at the Royal Netherlands Meteorological Institute (KNMI) and the SeaWinds-NOAA is a near-real-time product that was issued by the National Oceanic and Atmospheric Administration (NOAA). The SeaWinds science product issued by the National Aeronautics and Space Administration (NASA) is not included in this study. However, [Portabella and Stoffelen, 2002b] find little statistical difference between collocated NASA and NOAA products.

The wind products compared in this paper are the same ones studied by Vogelzang et al. [2011]. However, the wind spectra calculated in that paper used all data from SeaWinds and ASCAT recorded in January 2009. Here we only use winds over the equatorial Pacific ($10^{\circ}\text{S} - 10^{\circ}\text{N}$) during January 2009. This region is subdivided into three longi-

tudinal zones (Figure 1): West Pacific (140°–180°E), Central Pacific (180°–220°E) and East Pacific (220°–260°E). The high sea surface temperatures in the equatorial Pacific give rise to frequent and heavy rainfall in the Inter-Tropical Convergence Zone (ITCZ), the South Pacific Convergence Zone (SPCZ), and over the West Pacific Warm Pool.

The paper is structured as follows. In section 2 the statistical tools of turbulence theory (energy spectrum, covariance function and second-order structure function), their inter-relationships, and how their connection with observations are described. The data are described in section 3. In section 4 we describe the procedures used to calculate structure functions and spectra from the scatterometer data, and the methodology used to compare wind products. The results are presented in section 5, and our conclusions and recommendations for further work are given in section 6.

2 Statistical tools

2.1 Structure functions, covariance functions and spectra.

There are three interrelated statistical quantities commonly used to describe turbulence: the velocity covariance function, the second-order structure function, and the energy spectrum. The following is adapted from Pope [2000]. Assume a homogeneous, turbulent flow in two dimensions (2D). The covariance between velocity component u_i at position \vec{x} and u_j at position $\vec{x} + \vec{r}$ is defined as

$$R_{ij}(\vec{r}) = \langle [u_i(\vec{x}) - \langle u_i \rangle] [u_j(\vec{x} + \vec{r}) - \langle u_j \rangle] \rangle, \quad (1)$$

where $\langle \cdot \rangle$ denotes an average over all position vectors \vec{x} in the domain, $\vec{r} = (r_x, r_y)$ is the separation vector, and $d\vec{r} = dr_x dr_y$. The structure function tensor is defined as the covariance of velocity differences

$$D_{ij}(\vec{r}) = \langle [u_i(\vec{x} + \vec{r}) - u_i(\vec{x})] [u_j(\vec{x} + \vec{r}) - u_j(\vec{x})] \rangle, \quad (2)$$

and the energy spectrum tensor is defined as the Fourier transform of the velocity covariance tensor

$$\Phi_{ij}(\vec{\kappa}) = \frac{1}{(2\pi)^2} \int_{-\infty}^{\infty} R_{ij}(\vec{r}) e^{-i\vec{\kappa} \cdot \vec{r}} d\vec{r}, \quad (3)$$

where $\vec{\kappa} = (\kappa_x, \kappa_y)$ is the wavenumber.

There is a great deal of information in (1)–(3), which is made simpler, though less complete, by removing all directional information. This information is removed by considering (half) the trace of the covariance, structure function and energy spectrum tensors, and averaging over all separation vectors \vec{r} such that $|\vec{r}| = r$

$$R(r) = \frac{1}{2} \oint [R_{11}(\vec{r}) + R_{22}(\vec{r})] r d\theta \quad (4)$$

$$D_2(r) = \frac{1}{2} \oint [D_{11}(\vec{r}) + D_{22}(\vec{r})] r d\theta, \quad (5)$$

and over all wavenumbers $\vec{\kappa}$ such that $|\vec{\kappa}| = k$

$$E(\kappa) = \frac{1}{2} \oint [\Phi_{11}(\vec{\kappa}) + \Phi_{22}(\vec{\kappa})] \kappa d\phi \quad (6)$$

where $d\vec{r} = r d\theta$ and $d\vec{\kappa} = \kappa d\phi$. In isotropic turbulence, $\{R_{ij}(\vec{r}), D_{ij}(\vec{r}), \Phi_{ij}(\vec{\kappa})\}$ is completely determined by $\{R(r), D_2(r), E(\kappa)\}$.

Isotropic turbulence relation. If the turbulence is isotropic and divergence-free, then the 2D divergence equation yields the relation

$$D_{22} = \frac{d}{dr} (rD_{11}) \quad (7)$$

which implies that if $D_{11} \sim r^\gamma$, then $D_{22} \sim r^\gamma$.

Equivalence of power-laws If the second-order structure function scales with spatial lag r as, say, $D_{11}(r) \sim r^\gamma$, then, if $0 < \gamma < 2$, the energy spectrum scales with wavenumber κ as $E_{11}(\kappa) \sim \kappa^{-p}$, where

$$p = \gamma + 1 \quad (8)$$

2.1.1 Physical interpretations

Divergence and vorticity. At small r , δu_1 is proportional to $\partial u_1 / \partial x_1$ (a component of the horizontal divergence) and δu_2 is proportional to $\partial u_2 / \partial x_1$ (a component of the horizontal vorticity). This suggests the interpretation that

- D_{11} is a measure of the mean-square divergence at scale r , and
- D_{22} is a measure of the mean-square vorticity at scale r .

Kinetic energy at scale r . The magnitude of D_{11} (and D_{22}) at scale r represents the energy contained in scales less than r . The argument goes as follows. Eddies of size much less than r can induce a large signal at \vec{x} or $\vec{x}' = \vec{x} + \vec{r}$, but not at both points simultaneously. Thus eddies smaller than r tend to induce a contribution to D_{11} which is of the order of their kinetic energy. On the other hand, eddies much greater than r tend to produce similar velocities at both \vec{x} and \vec{x}' , and so make little contribution to the velocity difference $\delta \vec{u}$. This suggests that the connection with the energy spectrum can be written as

$$D_{11}(r) \approx \int_{\kappa \sim \pi/r}^{\infty} E_{11}(\kappa) d\kappa \quad (9)$$

and similarly for D_{22} .

Recently Davidson and Pearson [2005] have criticized the above interpretation as being too naive and argue that the right hand side of (9) should include a contribution from the enstrophy in eddies of size $> r$. However, in this paper we shall assume that the conventional interpretation is sufficient.

2.2 Connecting with observations

Observations can obtain an approximation to $R_{ij}(\vec{r})$ along a line. Consider a horizontal plane and suppose that measurements of the velocity vector $\vec{u}(\vec{r})$ are made along a line parallel to the x_1 axis in the (x_1, x_2) coordinate system. Let \hat{e}_1 and \hat{e}_2 denote the unit vectors along x_1 and x_2 , respectively. Then $\vec{r} = \hat{e}_1 r_1$, $\vec{\kappa} = \hat{e}_1 \kappa_1$, $u_1 = \vec{u} \cdot \hat{e}_1$,

$u_2 = \vec{u} \cdot \hat{e}_2$. The directional one-dimensional covariance and structure functions for velocity component u_2 are

$$R_{22}(\hat{e}_1 r_1) = \sigma_2^2 \rho_2(\hat{e}_1 r_1) \quad (10)$$

$$D_{22}(\hat{e}_1 r_1) = 2\sigma_2^2 [1 - \rho_2(\hat{e}_1 r_1)] \quad (11)$$

where

$$\sigma_2^2 = R_{22}(0) \quad (12)$$

is the variance of u_2 , and

$$\rho_2(\hat{e}_1 r_1) = R_{22}(\hat{e}_1 r_1)/R_{22}(0) \quad (13)$$

is its spatial autocorrelation function.

The one-dimensional spectra are defined to be twice the one-dimensional Fourier transform of $R_{22}(\hat{e}_1 r_1)$. Furthermore, since $R_{22}(\hat{e}_1 r_1)$ is real and an even function of r_1 , we can write

$$E_{22}(\hat{e}_1 \kappa_1) = \frac{2}{\pi} \int_0^\infty R_{22}(\hat{e}_1 r_1) \cos(\kappa_1 r_1) dr_1 \quad (14)$$

with the inversion formula

$$R_{22}(\hat{e}_1 r_1) = \int_0^\infty E_{22}(\hat{e}_1 \kappa_1) \cos(\kappa_1 r_1) d\kappa_1. \quad (15)$$

Setting $r_1 = 0$ in (15), we find

$$\sigma_2^2 = R_{22}(0) = \int_0^\infty E_{22}(\hat{e}_1 \kappa_1) d\kappa_1. \quad (16)$$

Finally, the energy spectrum and structure function are related by

$$D_{22}(\hat{e}_1 r_1) = 2 \int_0^\infty E_{22}(\hat{e}_1 \kappa_1) [1 - \cos(\kappa_1 r_1)] d\kappa_1 \quad (17)$$

Note that

$$D_{22} \rightarrow 2\sigma_2^2 \quad \text{as} \quad r_1 \rightarrow \infty. \quad (18)$$

2.2.1 Closer to reality: sampled data

In practice estimates of spectra and covariances are calculated using a set of discrete measurements. Consider measurements of a geophysical variable, m , taken along a linear transect at a set of uniformly spaced locations:

$$m_i = m(x_i), \quad x_i = i\Delta, \quad i = 0, \dots, N-1 \quad (19)$$

The mean and variance of m are

$$\bar{m} = \frac{1}{N} \sum_{i=0}^{N-1} m_i \quad (20)$$

$$\sigma_m^2 = \frac{1}{N} \sum_{i=0}^{N-1} (m_i - \bar{m})^2. \quad (21)$$

The spectrum is defined as the Fourier transform of the autocovariance function, but in practice is calculated from the discrete Fourier transform. The discrete Fourier transform of $m(x)$ and its inverse $M(k)$ are given by

$$M_l = M(k_l) = \Delta \sum_{j=0}^{N-1} m_j e^{i2\pi j l/N} \quad (22)$$

$$m_j = m(x_j) = \frac{1}{N\Delta} \sum_{l=-N/2}^{N/2} M_l e^{-i2\pi j l/N} \quad (23)$$

where M_l ($l = 0, \dots, N-1$) are the (dimensional) Fourier amplitudes, defined on a regular grid in k -space with spacing $(N\Delta)^{-1}$ at spatial frequencies $k_l = l(N\Delta)^{-1}$, $l = -N/2, \dots, N/2$. The one-sided spectrum is estimated by

$$\psi_l = \begin{cases} \frac{1}{N\Delta} |M_0|^2 \\ \frac{1}{N\Delta} [|M_l|^2 + |M_{-l}|^2], & l = 1, \dots, \frac{N}{2} - 1 \\ \frac{1}{N\Delta} |M_{N/2}|^2 \end{cases} \quad (24)$$

Parseval's theorem requires that

$$\frac{1}{N} \sum_{j=0}^{N-1} m_j^2 = \frac{1}{N\Delta} \sum_{l=0}^{N/2} \psi_l \quad (25)$$

and hence

$$\bar{m}^2 = \frac{1}{N\Delta} \psi_0 \quad (26)$$

$$\sigma_m^2 = \frac{1}{N\Delta} \sum_{l=1}^{N/2} \psi_l \quad (27)$$

Finally, the covariance and structure functions for m are

$$R_m(n\Delta) = \frac{1}{N-n} \sum_{i=0}^{N-n-1} [m_i(x_i) - \bar{m}] [m_i(x_i + n\Delta) - \bar{m}] \quad (28)$$

$$D_m(n\Delta) = 2 [\sigma_m^2 - R_m(n\Delta)] \quad (29)$$

3 Scatterometer Data

Scatterometers. The SeaWinds scatterometer on board the NASA QuikSCAT satellite is a rotating pencil-beam scatterometer operating at Ku-band (13.4 GHz) [Tsai et al., 2000]. The QuikSCAT mission measured windvectors from June 19, 1999 until November 23, 2009.

The ASCAT scatterometer on board the MetOP-A satellite is equipped with three arms, each with two radar antennas, and operates at C-band (5 GHz) [Figa-Saldaña et al., 2002]. MetOp-A was launched in 2006 and is operated by the European Organisation for the Exploitation of Meteorological Satellites (EUMETSAT).

Data and study region. This study uses scatterometer winds recorded in January 2009 for the equatorial Pacific from 10°S – 10°N and 140°–260°E (Figure 1). The data was subdivided into three regions:

- West Pacific (140°-180°E);
- Central Pacific (180°-220°E);
- East Pacific (220°-260°E).

For both spectra and structure functions, the whole swath of ASCAT and SeaWinds is taken into consideration, including the outer and nadir parts of the SeaWinds swath. Table 1 lists the four wind products and their root-mean-square precision [Vogelzang et al., 2011] for the zonal (u) and meridional (v) components:

SeaWinds-NOAA is obtained from NOAA. Ambiguity removal is carried out using a sophisticated spatial filtering algorithm called Direction Interval Retrieval with Thresholded Nudging (DIRTH) [Stiles et al., 2002]. The SeaWinds observation geometry varies across its swath. This gives rise to broad minima in the GMF, which results in larger wind direction retrieval errors and hence a noisier product. The noise is more prominent in u than in v . The spatial filter contained in DIRTH is believed to introduce some spatially correlated noise [Vogelzang et al., 2011].

SeaWinds-KNMI is a reprocessing of SeaWinds-NOAA using improved (rain) quality control [Portabella and Stoffelen, 2002a] and 2DVAR for ambiguity removal in combination with the Multiple Solution Scheme (MSS) to suppress the noise caused by broad minima in the GMF, particularly for nadir view [Vogelzang et al., 2009].

ASCAT-12.5 and ASCAT-25 can be found on the OSI SAF web pages at KNMI (www.knmi.nl/scatterometer). Due to the simpler ASCAT observation geometry, the GMF has well-defined minima and hence lower noise. The ASCAT products use 2DVAR for ambiguity removal.

SeaWinds-NOAA is already collocated with NWP forecasts from the model of the National Center for Environmental Prediction (NCEP). The ASCAT and SeaWinds-KNMI products are collocated with NWP forecasts from the model of the European Centre for Medium range Weather Forecasting (ECMWF).

Rain. Rain both attenuates and scatters the microwave signal through Rayleigh scattering. As the rain rate increases, the radar sees less of the radiation scattered by the surface and more of the radiation scattered by the rainy layer that becomes optically thicker due to the volumetric Rayleigh scattering [Boukabara et al., 2000]. The higher the frequency of the radar, the larger is the impact of rain attenuation and scattering.

The winds derived from SeaWinds are degraded by the presence of rain. Therefore, rain-flagged wind vectors were excluded from the analysis. The winds derived from ASCAT are largely unaffected by rain [see Portabella et al., 2011], but are susceptible to secondary effects. In heavy rain conditions the rain drops hitting the surface increases sea surface roughness. This ‘splashing’ effect increases the radar backscatter, which in turn affects the quality of wind speed and direction retrievals. Another effect associated

with heavy rain is increased wind variability. Convective rain cools the air below and reinforces downdraft near convective cells. These downdrafts often hit the ocean surface and cause outflow over the ocean, leading to variable wind speeds and directions. Such variability increases the isotropy of the radar backscattering at the ocean surface, yielding lower quality wind retrievals. These secondary effects of rain are a source of geophysical noise.

4 Methodology

The SeaWinds and ASCAT scatterometers measure the normalized radar cross section of the ocean surface. The cross sections are averaged on an approximately regular grid with size Δ approximately equal to 12.5 km or 25 km. This swath grid is inclined at an angle to the North-South axis that depends on latitude and on whether the satellite is on the ascending pass (South to North) or descending pass (North to South). The swath inclination angle is given by $\alpha = \arctan(1/\cos\phi \tan\Theta)$, where ϕ is the latitude, and $\Theta = 98.62^\circ$ is the satellite inclination angle of both the MetOp-A and QuikSCAT satellites; α is positive (negative) for an ascending (descending) pass.

Wind vector samples were selected for an *along-swath analysis*. That is, they are extracted from columns of the swath grid, meaning that they have the same cross-swath Wind Vector Cell (WVC) index. Samples from both the ascending and descending passes of the satellite were used. Wind vectors in a sample that had latitudes and longitudes outside the region of interest were flagged as missing. Wind vectors that did not pass quality control were also flagged as missing. In the case of SeaWinds-NOAA, this meant that all WVCs identified as containing rain were flagged missing. In the case of ASCAT winds, wind vectors were flagged missing if the monitoring flag, the KNMI quality control flag or the variational quality control flag was set [see KNMI, 2011, section 6.2].

The analysis is carried out in a cartesian coordinate system, denoted by (x_1, x_2) and oriented so that x_1 is the measurement axis. Wind vectors are transformed to wind components (u_1, u_2) at discrete locations along the measurement axis. In an along-swath analysis, the measurement axis is the along-swath axis x_a .

The component structure functions were calculated as follows. For a given sample, the velocity difference at separation r for wind component i was formed, squared and summed. This operation was repeated for each sample and the results averaged to obtain:

$$D_{ia}(r) = \frac{1}{N(r)} \sum_{n=1}^{N(r)} [u_i(x_{1n} + r) - u_i(x_{1n})]^2 \quad (30)$$

where $N(r)$ is the number of valid pairs at separation r , and, to simplify notation, the subscript a is used to denote the measurement axis is along-swath.

In order to calculate the spectra of a large number of samples in a reasonable time, it was necessary to apply additional criteria. First, samples were tested for the number of wind vectors they contained. A sample was rejected if it had fewer wind vectors than the Fast Fourier transform algorithm required: 128 for ASCAT-12.5 or 64 for the 25 km wind products. Next, samples were tested for missing data. A sample was rejected if it had too many gaps; otherwise missing values were replaced by an interpolated

value. The samples passing these tests were detrended by subtracting a linear function such that the first and last points of the sample have the same value. Then spectra were calculated and the average spectrum was calculated. In the tropics, the above procedure eliminates many samples from SeaWinds.

Spectral amplitudes ψ_j are shown as a function of spatial frequency k , rather than wavenumber. They are related by $\psi_{iia} dk \equiv E_{iia} d\kappa$.

We have settled on the following measures to compare spectra and structure functions:

Slopes. Spectral and structure function slopes can be compared using the slopes obtained from fits in log-log space. Both spectra and structure functions approach power-law behavior. The standard comparison is with the Kolmogorov scaling exponent. However, the range over which a power-law can be found is not always clear. At large scales the slopes approach those found for NWP models, while at small scales (less than 100 km), the effects of spatial filtering and noise can be seen. The range 50 – 250 or 300 km is the range where scatterometers resolve more structure than NWP. This also corresponds to the meteorological meso-beta scales [Orlanski, 1975]. Therefore, slopes are calculated and compared for this range of scales.

Ratios ψ_{22}/ψ_{11} and D_{22}/D_{11} . The ratio of component spectra ψ_{22}/ψ_{11} or structure functions D_{22}/D_{11} can be used to distinguish between turbulence generated by vortical modes from turbulence generated by divergent modes (gravity waves). Lindborg [2007] showed that if the turbulence were due to a 2D incompressible vorticity field, then $\psi_{22}/\psi_{11} = D_{22}/D_{11} = 5/3$, and if due to a gravity wave field, then $\psi_{22}/\psi_{11} = D_{22}/D_{11} = 3/5$. The intermediate case, vorticity equals divergence, is given by $\psi_{22}/\psi_{11} = D_{22}/D_{11} = 1$. When making these comparisons, it must be remembered that they are only calculated here for the along-swath direction.

Representation error. The representation error is defined as the variance missed by the NWP model, but captured by scatterometer measurements. [Vogelzang et al., 2011] calculate the representation error by integrating the difference between scatterometer and NWP spectra:

$$RE_{iia}^{\psi}(k_{NWP}) = \int_{k_{NWP}}^{k_{scat}} [\psi_{iia}^{scat}(k) - \psi_{iia}^{NWP}(k)] dk \quad (31)$$

where ψ_{iia}^{scat} and ψ_{iia}^{NWP} are, respectively, the scatterometer and NWP wind spectra. The upper integration limit in (31) is the highest spatial frequency observed by the scatterometer, $k_{scat} = 1/2\Delta$. The spatial scale associated with k_{scat} is 2Δ , which is generally close to the actual spatial resolution of the scatterometer winds. The lower integration limit in (31) corresponds to the spatial frequency k_{NWP} at which the numerical cutoff in the NWP model starts to suppress small scales. The spatial scale associated with k_{NWP} is

$$s_{NWP} = \frac{1}{k_{NWP}} \quad (32)$$

One expects s_{NWP} to be determined only by the characteristics of the NWP model.

The representation error can also be calculated from structure functions based on the interpretation that $D_{ii}(r) \sim [\text{energy in eddies of size } < r]$. Thus the structure function representation error is calculated as the difference between scatterometer and NWP structure functions at scale s_{NWP} :

$$RE_{ii}^D(s_{NWP}) = \frac{1}{2} (D_{ii}^{scat}(s_{NWP}) - D_{ii}^{NWP}(s_{NWP})) \quad (33)$$

where the 1/2 on the right-hand side is written because of Eq. (18).

5 Results

5.1 Tropical Pacific rain

An indicator of geophysical forcing associated with rain and its spatial variability over the Tropical Pacific is provided by measurements of rain rate by the radiometer carried on the Tropical Rainfall Measuring Mission (TRMM) satellite. The spatial and monthly variability of Tropical Pacific rain during the 12 month period November 2008 to October 2009 is illustrated in Figure 2 (data obtained from Remote Sensing Systems (<http://www.ssmi.com>)). The figure shows latitude-time plots of monthly and zonally averaged rain rate for the West, Central and Pacific regions. The ITCZ can be identified as a band of heavy rain that persists (or nearly so) throughout the year in the Central and East Pacific between 5°N and 15°N. In the West Pacific, heavy rain is distributed in a bimodal fashion from November to June, with peak intensities in the ITCZ north of the equator and in the SPCZ south of the equator. From June to October heavy rain is more uniformly distributed between 15°S and 15°N, with a lobe that extends northward to 25°N; the latter is associated with the strong convective activity occurring in the monsoon trough during the East Asian Monsoon.

Focussing on the month of January 2009 in the region of latitudes 10°S and 10°N, Fig. 2 shows that rain was heavy throughout those latitudes in the West Pacific, and heavy mainly between 5° and 10°N in the Central and East Pacific.

Since SeaWinds is very sensitive to rain, Fig. 2 gives an excellent indication of the expected regional and seasonal variations in the quality of SeaWinds-NOAA and SeaWinds-KNMI products.

5.2 Spectra

Figure 3 shows the number of valid samples for each wind product in each region, that spectra could be calculated for. Rain contamination (Fig. 2) resulted in only a small number of valid SeaWinds samples. Because the East Pacific has much less rain, more valid samples were found for that region than either the West or Central Pacific. However, due to the rain in the ITCZ, there are still far fewer samples than for ASCAT.

There are about twice the number of valid ASCAT-12.5 samples as ASCAT-25 samples, a simple consequence of a smaller grid. Land is present in the West Pacific region. This caused a large reduction in the number of valid ASCAT samples. Because land was concentrated in the western half of the region, the sampling is biased and wind spectra only reflect the turbulence in the eastern half of the region. If the turbulence is

homogeneous within the West Pacific region, then this will have no important effect on the results. However, as will be seen, the turbulence is inhomogeneous.

Wind spectra are shown in Figure 4 for the along-swath (top) and cross-swath (bottom) components. Scatterometer spectra are the solid lines and NWP spectra, for the same sampling, are the dashed lines. The wind products are color coded: ASCAT-12.5 (black), ASCAT-25 (blue), SeaWinds-KNMI (green), SeaWinds-NOAA (red). This color coding is used in all figures. Fig. 4 is used here. Theoretical $k^{-5/3}$ and k^{-3} spectra are shown as thick black lines. The vertical line segments indicate the meso-beta range.

The consequence of the small number of acceptable SeaWinds samples are complex and noisy spectra, indicating poor convergence. As a result, SeaWinds spectra are not considered further.

Fig. 4 shows that ASCAT spectra are well-converged. ASCAT-25 spectra lie on top of ASCAT-12.5 spectra down to $\sim 4 \times 10^{-6}$ m (250 km) and then drop away. The difference in the ASCAT spectra was investigated by Vogelzang et al. [2011], who showed that ASCAT-12.5 resolves smaller scales than ASCAT-25 at the cost of only a little noise.

Ratios ψ_{22a}/ψ_{11a} . Spectral ratios ψ_{22a}/ψ_{11a} (ASCAT winds) are shown in Figure 5. Interestingly, the ratios are independent of r and close to 0.5 in each region. This shows that there is much less variability in the zonal than the meridional wind component. Actually this is the equatorial waveguide effect near the equator. The value of the ratio suggests that the turbulence is dominated by divergent modes (i.e., gravity waves).

Spectral slopes. Spectral slopes were calculated from a linear fit in log-log space to the spectral amplitudes with spatial frequencies in the meso-beta scales. The spectral slopes are shown in Table 2.

Representation error. NWP and ASCAT spectra (Fig. 4) are parallel down to $\sim 2 \times 10^{-6}$ m $^{-1}$ (500 km), after which NWP spectra drop off sharply, following an approximate k^{-3} power-law. This missing NWP variance is quantified by the representation error RE_{ii}^{ψ} (Eq. (31)) and shown in Figure 6. The results are nearly the same for each region and shows that ASCAT-12.5 is further from NWP than ASCAT-25. Furthermore, $RE_{11a}^{\psi} > RE_{22a}^{\psi}$, meaning that most of the missing NWP variance is in the meridional wind component.

5.3 Structure functions

Figure 7 shows the number of velocity differences that contribute to the average at each r . For comparison with the number of spectra shown in Fig. 3, suppose that velocity differences were only formed from the samples used to compute spectra. Then one finds that the number of velocity differences shown in Fig. 7 for the West Pacific represent an increase of 2 to 3 times for ASCAT-winds, and an increase of more than 50 times for SeaWinds-winds. This makes clear that the structure function calculation makes better use of the available data.

The longitudinal (D_{11a}) and transverse (D_{22a}) structure functions are shown in Figure 8. The scatterometer structure functions are the solid lines and the NWP structure

functions are the dashed lines. The thick solid lines are theoretical $r^{2/3}$ and r^2 structure functions, and the vertical line segments indicate the meso-beta range.

Fig. 8 demonstrates that because the structure function method makes better use of the data, the SeaWinds-KNMI and SeaWinds-NOAA structure functions are well converged. Thus it is now possible to compare ASCAT and SeaWinds products.

There are two subranges where the differences between products are most important and most interesting: the meso-beta range (say 300 to 50 km) and the small r range ($r < 100$ km).

Small r . Fig. 8 shows that at small r (< 100 km) the structure functions show distinct and different shapes that reflect both noise level and spatial filtering. ASCAT wind products have a downward bend, with ASCAT-12.5 having a stronger bend than ASCAT-25. SeaWinds products have an upward bend, strongest in the West Pacific and weakest in the East Pacific; in fact, SeaWinds-KNMI appears to be perfectly straight in the East Pacific.

First recall that $D_{ii}(r) \sim$ at scale r represents the kinetic energy held in scales less than r and that D_{ii} can be used to provide a comparison at small r . Ordering by D_{11a} shows that in all regions

$$\text{ASCAT-12.5} > \text{ASCAT-25} > \text{SeaWinds-NOAA} > \text{SeaWinds-KNMI}$$

This ordering reflects the ability of ASCAT-12.5 to resolve small scale features better than ASCAT-25, ASCAT winds to resolve better than SeaWinds, SeaWinds to be heavily filtered at small r , but also that SeaWinds-NOAA has more noise than SeaWinds-KNMI.

Ordering by D_{22a} is different. In the West Pacific:

$$\text{SeaWinds-NOAA} > \text{ASCAT-12.5} > \text{ASCAT-25} > \text{SeaWinds-KNMI};$$

in the Central Pacific:

$$\text{SeaWinds-NOAA} > \text{ASCAT-12.5} > \text{SeaWinds-KNMI} > \text{ASCAT-25};$$

and in the East Pacific:

$$\text{SeaWinds-NOAA} > \text{ASCAT-12.5} > \text{ASCAT-25} > \text{SeaWinds-KNMI},$$

which is the same as in the West Pacific.

It is unreasonable to expect SeaWinds-NOAA to resolve and represent small scale kinetic energy better than ASCAT-12.5 in regions with large amounts of rain. Therefore, the suggestion is that the position of SeaWinds-NOAA in the D_{22a} ordering is because it has a very large noise level. The position of SeaWinds-KNMI has exchanged with ASCAT-25 in the Central Pacific. The reason is not clear, but probably related to the fact that the Central Pacific is a transition region.

Ratios D_{22a}/D_{11a} . Figure 9 shows the ratio D_{22a}/D_{11a} as a function of r for scatterometer winds (top panels) and, for reference, NWP winds (bottom panels). In the Central and East Pacific, the ASCAT ratios are approximately constant and less than

one. Both SeaWinds products are in agreement with ASCAT for $r \gtrsim 300$ km, but increase sharply as r decreases to a value near or greater than one. Due to the large noise level in the SeaWinds zonal wind component, their D_{22a}/D_{11a} ratios at small r should be treated as an artifact.

In the West Pacific a much larger difference is found between SeaWinds and ASCAT. The SeaWinds-NOAA ratio implies that vorticity dominates over divergence at all scales. On the other hand, both ASCAT ratios imply that vorticity dominates over divergence in the intermediate and large scales, but in the small scales divergence dominates over vorticity. Because the West Pacific is a region dominated by convection at small scales, but is also a region that generates large-scale vorticity, the ASCAT ratios make physical sense.

According to turbulence theories, turbulence generated mainly by gravity waves will have a ratio less than one and turbulence generated mainly by vortical modes will have a ratio larger than one. Thus the conclusion is that the turbulence in the Central and East Pacific, where there is little small scale convection, is dominated by gravity waves. This is consistent with Cho et al. [2001], who analyzed winds measured by research aircraft during the Pacific Exploratory Mission in the Tropics. The turbulence in the West Pacific has characteristics of gravity modes at small scales and vortical modes at large scale. Finally, the noise in the SeaWinds products produce spurious small scale vorticity in the measured wind field.

Structure function slopes. Structure function slopes (γ_{11a} and γ_{22a}) obtained from linear fits in log-log space to D_{11a} and D_{22a} in the meso-beta range are given in Table 3. Note that the ordering of the slopes for each region and each component are the reverse of the small r ordering of structure function magnitudes described above. This implies that the slopes are influenced by noise and spatial filtering, with noise causing smaller and filtering steeper slopes.

Representation error Figure 10 shows the structure function representation error RE_{iia}^D , calculated using Eq. (33). The ASCAT results are similar to the those obtained from the spectral representation error. Table 4 shows an attempt to rank the structure function representation error using the value near the upper limit of the meso-beta range (i.e., $r \approx 300$ km); only rankings for the West and East Pacific are given. The RE_{11a}^D rankings clearly show ASCAT-winds furthest and SeaWinds-winds closest from NWP in all regions. The same is found for RE_{22a}^D rankings in the East Pacific. However, in the West Pacific, RE_{22a}^D rankings identify SeaWinds-NOAA as furthest and SeaWinds-KNMI closest to NWP.

6 Conclusions and Recommendations

In this study SeaWinds and ASCAT winds over the equatorial Pacific were compared using wind spectra and structure functions. Due to the large amount of rain in the equatorial region, there were few SeaWinds samples that could be used to compute spectra. Therefore, only ASCAT winds could be used to compare spectra and structure

functions. On the other hand, because structure functions make efficient use of all available data, all winds were compared using structure functions.

In theory, spectra and structure functions should yield equivalent results. However, because spectra require sample lengths with few missing data, the samples were not the same as used to calculate structure functions. Missing data due to the presence of land (Indonesia) is responsible for the smaller number of samples accepted to calculate ASCAT spectra for the West Pacific (Fig. 3). Since land is only in the western portion of the West Pacific box, results from spectra only represent behavior in the eastern half.

Theory predicts that the ratios ψ_{22a}/ψ_{11a} and D_{22a}/D_{11a} should be equal. Comparison of Figs. 5 and 9 show that the ratios are in good agreement for both the Central and East Pacific, but in disagreement for the West Pacific. To understand why, consider the wind fields in Figure 11. The top half of the figure shows a typical January wind field for the Tropical Pacific, measured by SeaWinds and superimposed on sea surface temperatures. A closer up view of the western Pacific for January 2009 is shown in the bottom half of the figure. (The latitude limits of the black box only go from 5°S to 5°N.) The eastern half of the West Pacific box is dominated by zonal winds, while the western half has a larger meridional component, caused by winds flowing into a strong convectively active region of the SPCZ. This makes clear why the spectral and structure function ratios disagree for the West Pacific region: namely that the turbulence is inhomogeneous. Future work should divide the West Pacific box into an east and west and calculate compare structure functions.

If an energy spectrum follows a k^{-p} power-law, the structure function should follow a r^γ power-law, where $\gamma = p - 1$ and $0 < \gamma < 2$. Comparison of ASCAT spectral and structure function slopes (Tables 2 and 3) shows that ASCAT-25 spectral slopes are typically a little larger and ASCAT-12.5 a little smaller than the structure function slopes. The disagreement is not too bad, though greater than one would hope. More comparison of spectra and structure functions in other regions using the exact same samples is recommended.

Finally, we note that the ASCAT spectral and structure function representation errors were in good agreement.

Because the structure function calculation is tolerant of missing data, well-resolved structure functions were obtained for all wind products in all regions. Structure functions at small r (< 100 km) demonstrated wind product-dependent shapes. The ordering of the magnitudes at small r reveal information about noise level and spatial filtering. The slopes in the meso-beta range were also found to demonstrate the effects of noise level and filtering. Comparison of representation error was consistent with Vogelzang et al. [2011], especially that the zonal component of SeaWinds-NOAA was an outlier.

6.1 Recommendations for further work

The work carried out here has led to a number of ideas for further work. The following is a partial list.

1. In this work only an along-swath analysis was carried out. This can easily be extended to a cross-swath analysis.
2. It was pointed out in section 2.1.1 that the longitudinal (transverse) structure

function gives a measure of the divergence (vorticity) at scale r . To examine this further, structure functions should be calculated for scatterometer rotation and divergence fields and a comparison made.

3. Rain detection and wind direction skill are tightly connected for SeaWinds. Both skills are best in the sweet swath. In order to assess the effect of eliminating rain-flagged WVCs on, for example, structure function slopes, future work should examine the effect of taking out the nadir WVCs.
4. Carry out structure function analysis of NWP fields, especially for the tropics.
5. It would be interesting and important to carry out structure function analysis of buoy winds, to characterize the meso-gamma scales and for scatterometer validation purposes.
6. Calculate structure functions for other oceanic regions.
7. Investigate smaller regions. This is possible because structure functions do not have a requirement on sample length. Some investigation has already been done and will be reported on in a second report.
8. Estimate noise levels. Structure functions should be identically zero at $r = 0$. By interpolating the structure functions to zero, an estimate of the noise level can be made as a function of geographical zone and time. Some work has already been done and will be reported on in a third report.
9. Third-order structure function analysis. Theory indicates that the direction of energy transfer by turbulence can be inferred by the sign of the third-order structure function. Some work has already been carried out and will be reported.
10. Extend the analysis to the full length of the scatterometer record.

References

- A. Babiano, C. Basdevant, and R. Sadourny. Structure Functions and Dispersion Laws in Two-Dimensional Turbulence. *J. Atmos. Sci.*, 42(9):941–949, 1985. doi: 10.1175/1520-0469(1985)042<0941:SFADLI>2.0.CO;2.
- S.A. Boukabara, R.N. Hoffman, and C. Grassotti. Atmospheric compensation and heavy rain detection for SeaWinds using AMSR. Technical report, Atmospheric Environmental Research Inc., 131 Hartwell Ave., Lexington, Massachusetts (USA), 2000.
- M. Bourassa, A. Stoffelen, H. Bonekamp, P. Chang, D. Chelton, J. Courtney, R. Edson, J. Figa, Y. He, H. Hersbach, K. Hilburn, Z. Jelenak, K. Kelly, R. Knabb, T. Lee, E. Lindstrom, W. Liu, D. Long, W. Perrie, M. Portabella, M. Powell, E. Rodriguez, D. Smith, V. Swail, and F. Wentz. Remotely Sensed Winds and Wind Stresses for Marine Forecasting and Ocean Modeling. In J. Hall and D. Harrison, D.E. & Stammer, editors, *Proceedings of OceanObs09: Sustained Ocean Observations and Information for Society (Vol. 2)*. ESA Publication WPP-306, 2010. doi: 10.5270/OceanObs09.cwp.08.

- John Y. N. Cho, Bruce E. Anderson, John D. W. Barrick, and K. Lee Thornhill. Aircraft observations of boundary layer turbulence: Intermittency and the cascade of energy and passive scalar variance. *J. Geophys. Res.*, 106, D23:32,469–32,479, 2001. doi: 10.1029/2001JD900079.
- P. A. Davidson and B. R. Pearson. Identifying turbulent energy distributions in real, rather than Fourier, space. *Phys. Rev. Lett.*, 95:214501, 2005. doi: 10.1103/PhysRevLett.95.214501.
- J. Figa-Saldaña, J.J.W. Wilson, E. Attema, R. Gelsthorpe, M.R. Drinkwater, and A. Stoffelen. The advanced scatterometer (ASCAT) on the meteorological operational (MetOp) platform: A follow on for the European wind scatterometers. *Can. J. Remote Sens.*, 28:404–412, 2002. doi: 10.5589/m02-035.
- KNMI. *ASCAT Wind Product User Manual*, 2011. URL www.osi-saf.org.
- Erik Lindborg. Horizontal Wavenumber Spectra of Vertical Vorticity and Horizontal Divergence in the Upper Troposphere and Lower Stratosphere. *J. Atmos. Sci.*, 64 (3):1017–1025, March 2007. doi: 10.1175/JAS3864.1.
- I Orlanski. A rational subdivision of scales for atmospheric processes. *Bull. Amer. Meteor. Soc.*, 56:527–530, 1975.
- S. B. Pope. *Turbulent Flows*. Cambridge University Press, 2000.
- M. Portabella and A. Stoffelen. A comparison of KNMI Quality Control and JPL Rain Flag for SeaWinds. *Can. J. Remote Sens.*, 28:424–430, 2002a.
- M. Portabella and A. Stoffelen. Characterization of residual information for SeaWinds quality control. *IEEE Trans. Geosci. Remote Sens.*, 40(12):2747–2759, dec 2002b. ISSN 0196-2892. doi: 10.1109/TGRS.2002.807750.
- M. Portabella, A. Stoffelen, W. Lin, A. Verhoef, J. Verspeek, J. Ballabrera, and A. Turiel. Rain effects on ASCAT retrieved winds: Towards an improved quality control. *IEEE Trans. Geosci. Remote Sens.*, Submitted, 2011.
- B.W. Stiles, B.D. Pollard, and R.S. Dunbar. Direction interval retrieval with thresholded nudging: A method for improving the accuracy of QuikSCAT winds. *IEEE Trans. Geosci. Remote Sens.*, 40:79–89, 2002.
- A. Stoffelen and M. Portabella. On Bayesian Scatterometer Wind Inversion. *IEEE Transactions on Geoscience and Remote Sensing*, 44:1523–1533, 2006. doi: 10.1109/TGRS.2005.862502.
- W.-T. Tsai, M. Spencer, C. Wu, C. Winn, and K. Kellogg. SeaWinds on QuikSCAT: sensor description and mission overview. In *Geoscience and Remote Sensing Symposium, 2000. Proceedings. IGARSS 2000. IEEE 2000 International*, volume 3, pages 1021–1023 vol.3, 2000. doi: 10.1109/IGARSS.2000.858008.

- J. Vogelzang, A. Stoffelen, A. Verhoef, J. de Vries, and H. Bonekamp. Validation of two-dimensional variational ambiguity removal on SeaWinds scatterometer data. *J. Atmos. Oceanic Technol.*, 26:1229–1245, 2009. doi: 10.1175/2008JTECHA1232.1.
- J. Vogelzang, A. Stoffelen, A. Verhoef, and J. Figa-Saldana. On the quality of high-resolution scatterometer winds. *J. Geophys. Res.*, 116:C10033, 2011. doi: 10.1029/2010JC006640.

Product	Grid Size (km)	u_{rms}	v_{rms} (ms^{-1})
ASCAT-12.5	12.5	0.7	0.8
ASCAT-25	25	0.7	0.7
SeaWinds-KNMI	25	0.8	0.6
SeaWinds-NOAA	25	1.2	1.1

Table 1: Wind products compared in this work. u_{rms} and v_{rms} taken from Vogelzang et al. [2011]

	West	Central Pacific	East
<i>p11a</i>			
ASCAT-25	2.35	2.91	2.38
ASCAT-12.5	1.48	1.67	1.63
<i>p22a</i>			
ASCAT-25	2.08	3.04	2.29
ASCAT-12.5	1.59	1.96	1.72

Table 2: Spectral slopes estimated from linear fits in log-log space in the meso-beta range of scales (indicated by the vertical line segments in Fig. 4).

West Pacific		Central Pacific		East Pacific	
γ_{11a}		γ_{11a}		γ_{11a}	
SeaWinds-KNMI	1.20	SeaWinds-KNMI	1.52	SeaWinds-KNMI	1.27
SeaWinds-NOAA	1.07	SeaWinds-NOAA	1.42	SeaWinds-NOAA	1.20
ASCAT-25	0.86	ASCAT-25	1.23	ASCAT-25	1.04
ASCAT-12.5	0.71	ASCAT-12.5	1.01	ASCAT-12.5	0.86
γ_{22a}		γ_{22a}		γ_{22a}	
SeaWinds-KNMI	1.28	ASCAT-25	1.19	SeaWinds-KNMI	1.17
ASCAT-25	1.14	SeaWinds-KNMI	1.07	ASCAT-25	1.10
ASCAT-12.5	0.98	ASCAT-12.5	0.97	ASCAT-12.5	0.94
SeaWinds-NOAA	0.90	SeaWinds-NOAA	0.82	SeaWinds-NOAA	0.86

Table 3: Rankings of structure function meso-beta range slopes (γ_{11a} , γ_{22a}) estimated from linear fits to (D_{11a} , D_{22a}) in log-log space.

$RE_{11a}^D(300 \text{ km})$	
West Pacific	East Pacific
ASCAT-12.5	ASCAT-12.5
ASCAT-25	ASCAT-25
SeaWinds-NOAA	SeaWinds-KNMI
SeaWinds-KNMI	SeaWinds-NOAA
$RE_{22a}^D(300 \text{ km})$	
West Pacific	East Pacific
SeaWinds-NOAA	ASCAT-12.5
ASCAT-12.5	ASCAT-25
ASCAT-25	SeaWinds-KNMI
SeaWinds-KNMI	SeaWinds-NOAA

Table 4: Rankings of the structure function representation error. Top-to-bottom are furthest-to-closest to NWP winds. Rankings are estimated by values at $r \approx 300 \text{ km}$.

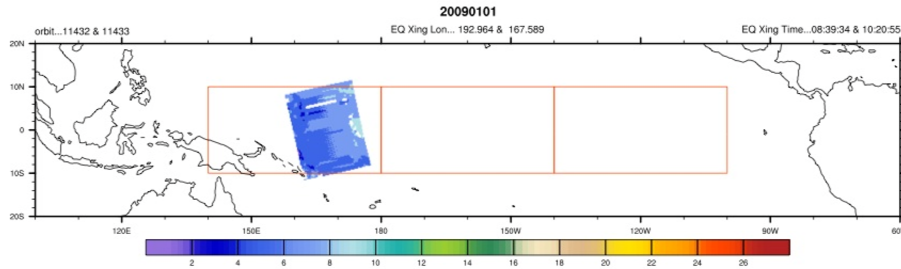


Figure 1: Study area in the Pacific — between latitudes 10°S and 10°N, divided into three longitudinal zones (West, Central and East Pacific).

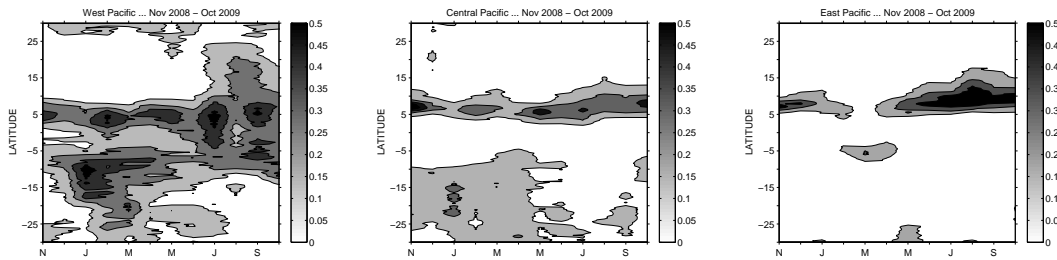


Figure 2: Latitude-time plots of the rain rate (mm/hr) for the period November 2008 – October 2009. The rain rate is averaged monthly and zonally: West Pacific (140 – 180 E), Central Pacific (180 – 220 E), and East Pacific (220 – 260 E). (TRMM Microwave Imager (TMI) rain rates downloaded from Remote Sensing Systems <http://www.ssmi.com>.)

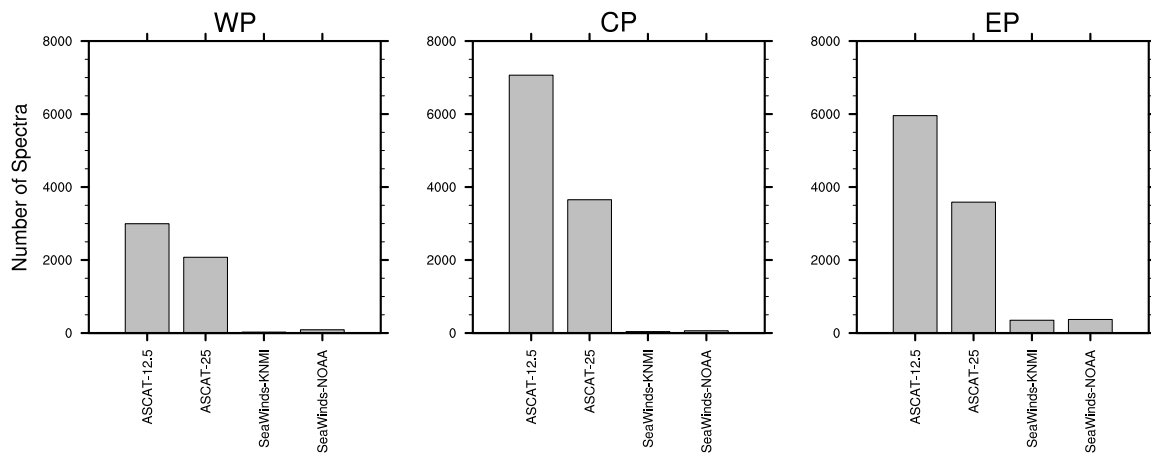


Figure 3: Number of spectra averaged to produce Fig. 4. The small number of SeaWinds samples is due to rain contamination, and the smaller number of ASCAT samples in the West Pacific is due to land (see Fig. 1).

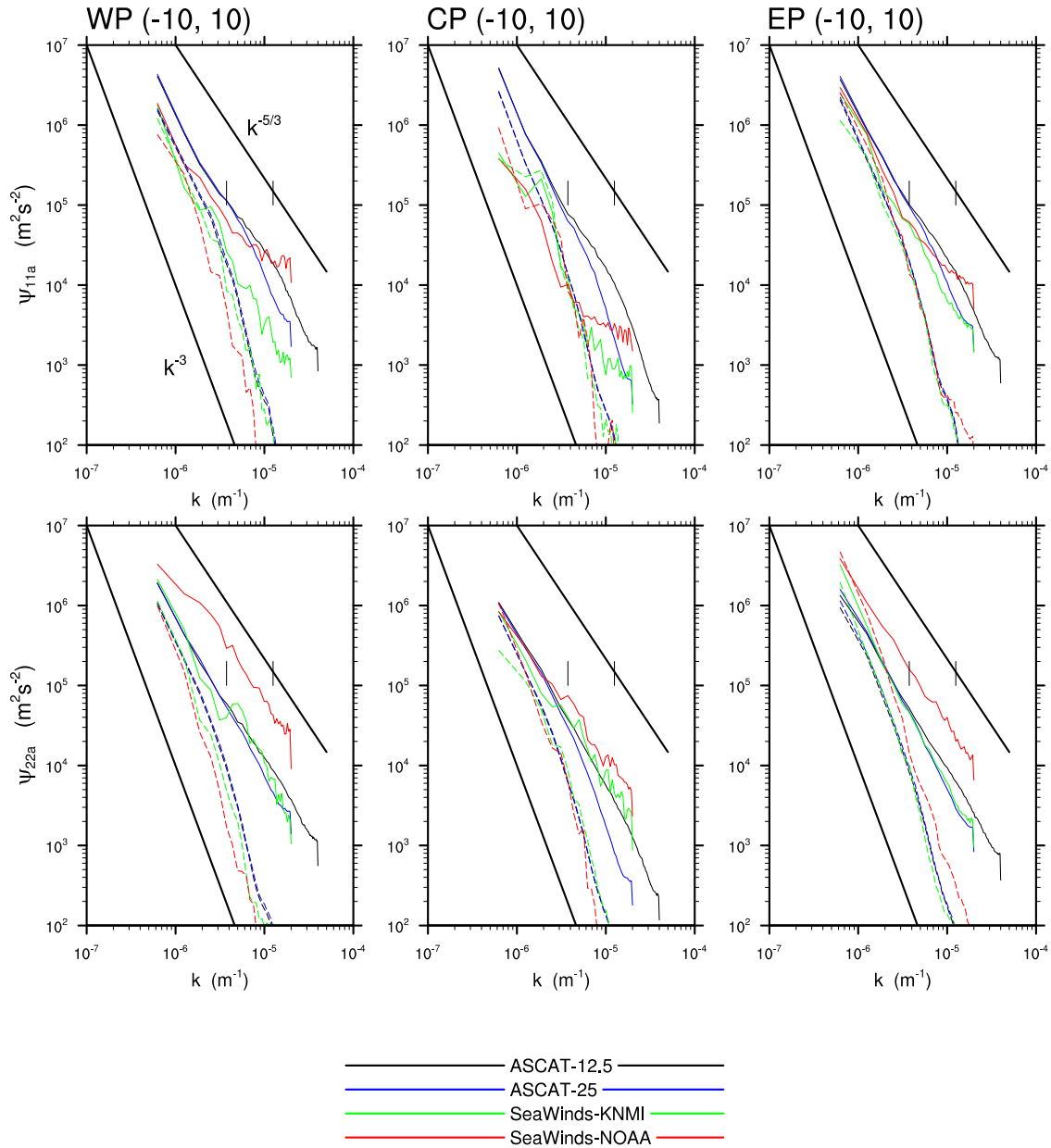


Figure 4: Wind spectra calculated using along-swath samples between latitudes 10°S and 10°N : Along-swath component wind spectra ψ_{11a} (top), and cross-swath component wind spectra ψ_{22a} (bottom). The dashed lines are spectra for the NWP background winds for the same sampling. The wind products are color coded: ASCAT-12.5 (black), ASCAT-25 (blue), SeaWinds-KNMI (green), SeaWinds-NOAA (red). Theoretical $k^{-5/3}$ and k^{-3} spectra are shown as thick solid lines. The vertical line segments indicate the meso-beta range.

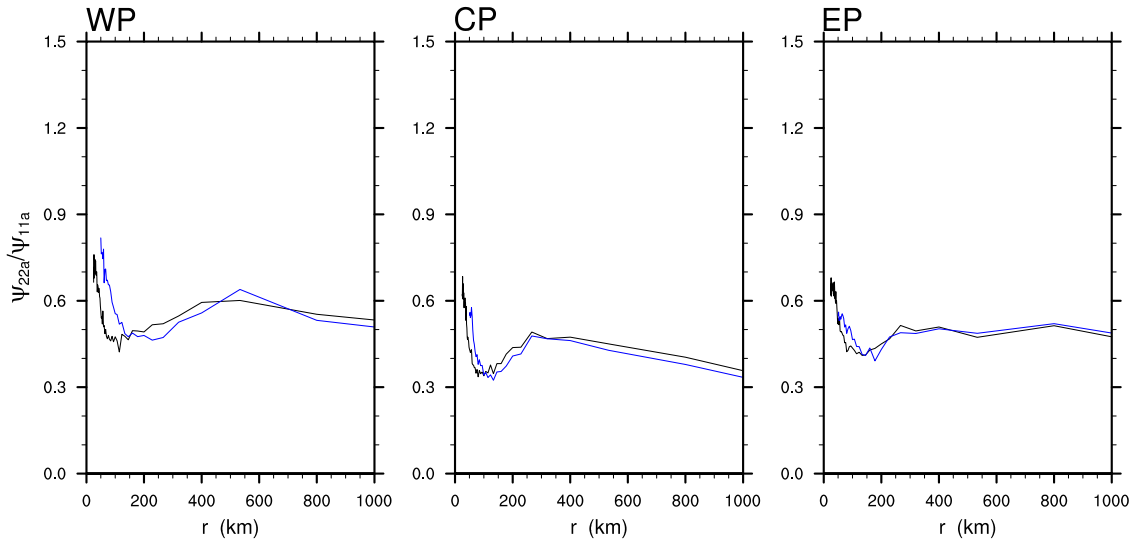


Figure 5: The spectral ratio ψ_{22a}/ψ_{11a} vs r for ASCAT-12.5 (black) and ASCAT-25 (blue).

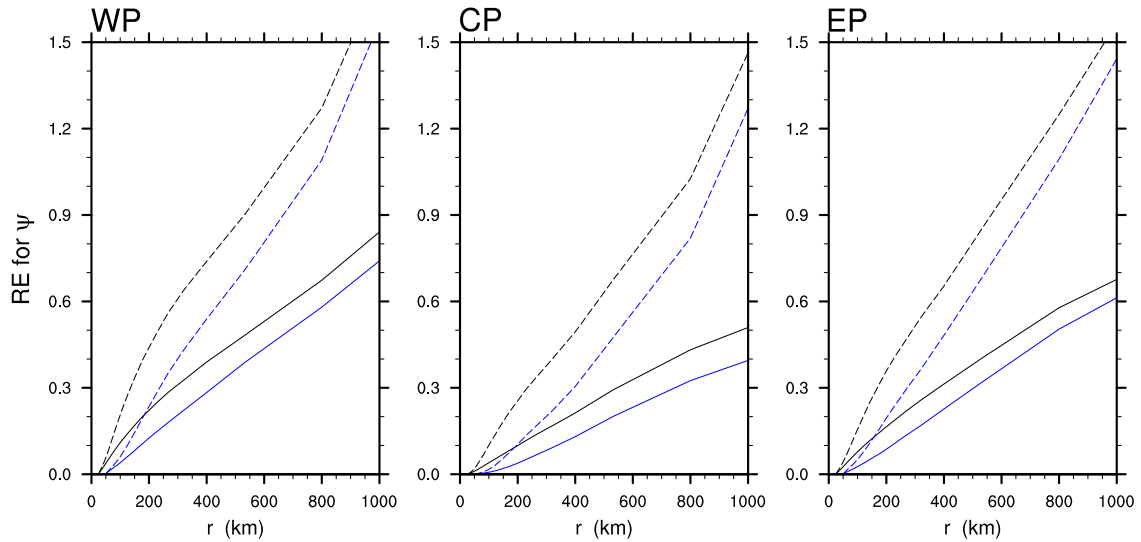


Figure 6: Representation error estimated from the spectra using Eq. (31): RE_{11a}^ψ (dashed) and RE_{22a}^ψ (solid) for ASCAT-12.5 (black) and ASCAT-25 (blue).

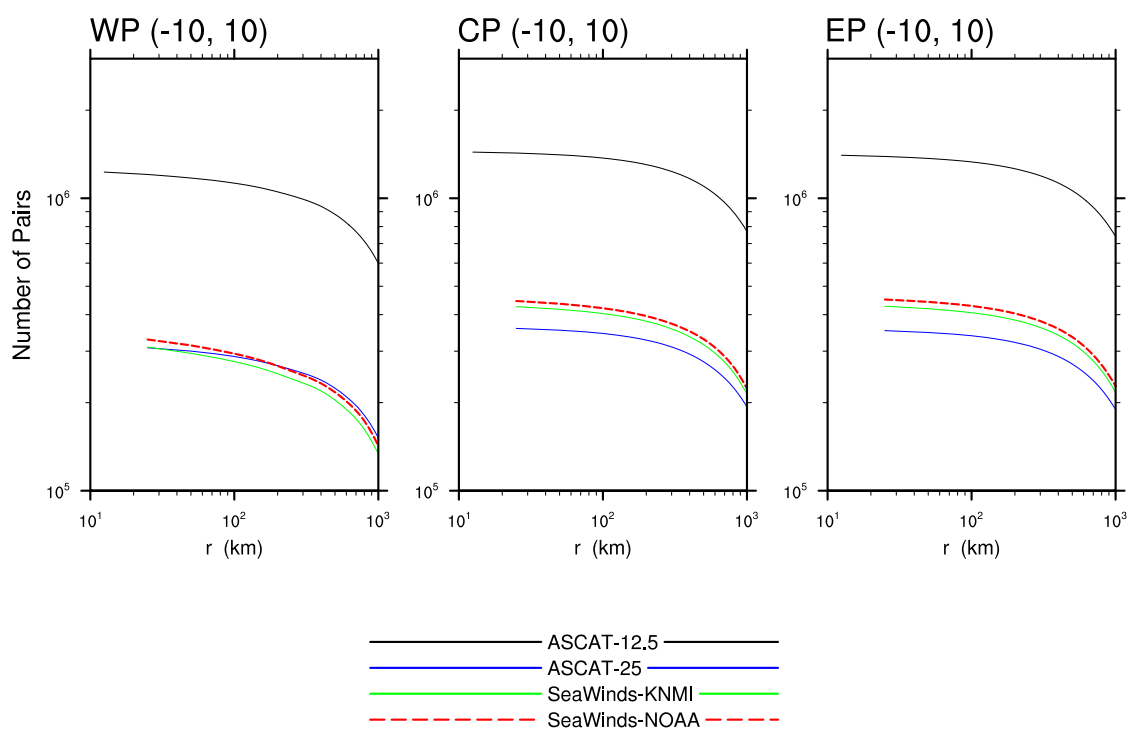


Figure 7: The number of pairs as a function of r used to calculate the structure functions shown in Fig. 8.

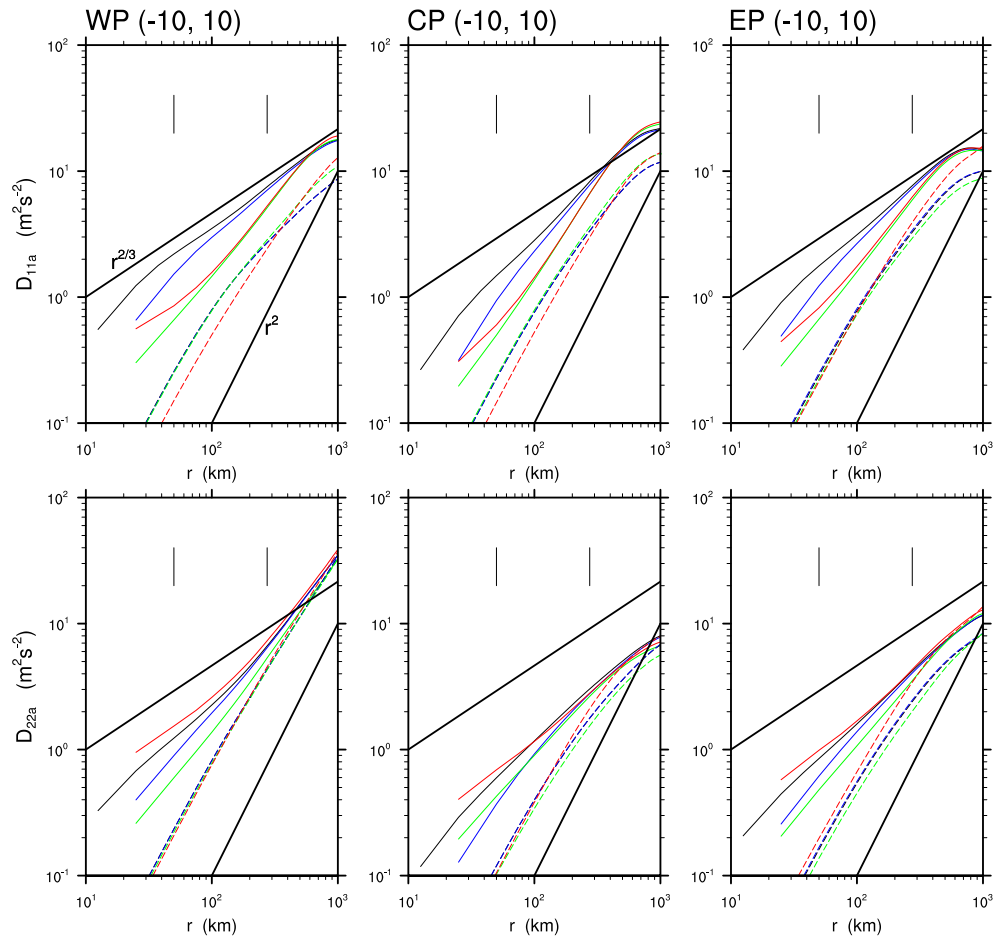


Figure 8: Second-order structure functions for latitudes 10°S – 10°N . Also shown are the structure functions for NWP background winds (dashed) for the same sampling. The thick solid lines are theoretical structure functions for $r^{2/3}$ and r^2 scaling.

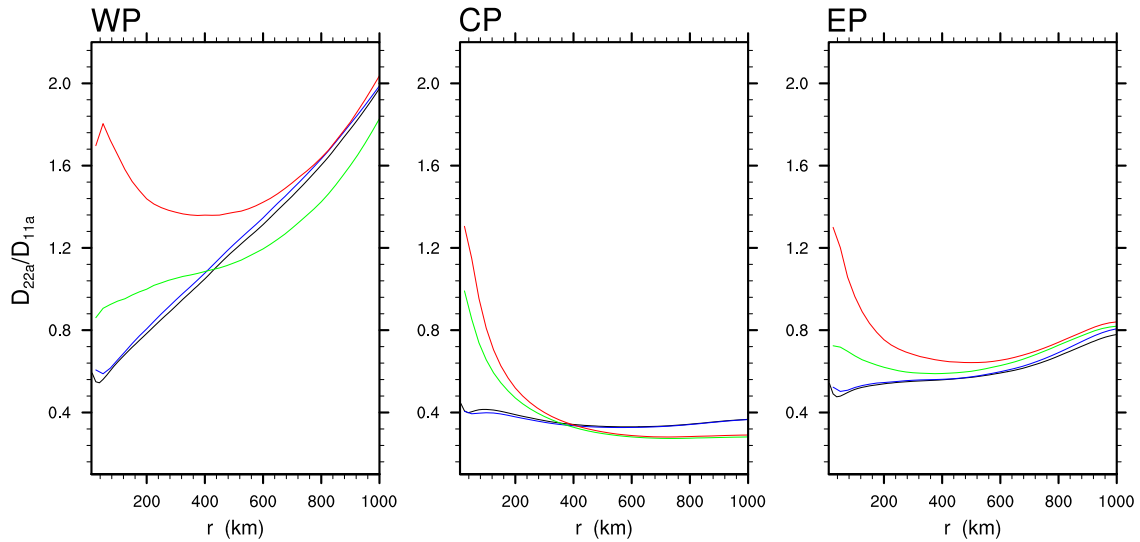


Figure 9: Structure function ratios D_{22a}/D_{11a} vs r . Compare with Fig. 5 and note the large difference in the spectral ratio for the West Pacific. This is due to sampling differences (see text).

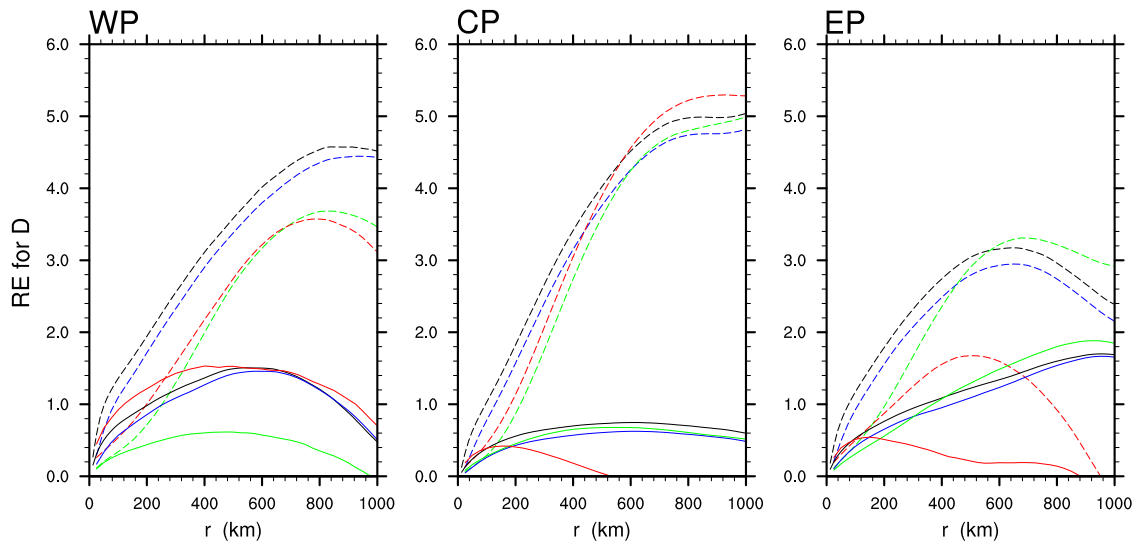


Figure 10: Representation error estimated from the structure functions shown in Fig. 8. Dashed lines are RE_{11a} and solid lines RE_{22a} . The color coding is as in previous figures.

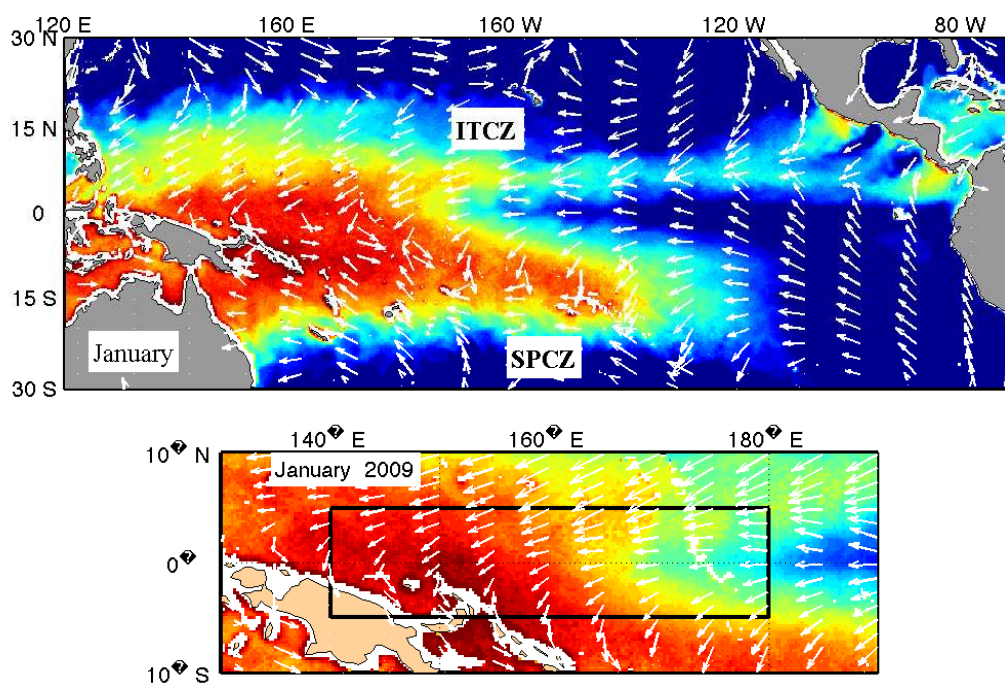


Figure 11: Equatorial winds superimposed on sea surface temperatures. Winds and sea surface temperatures are January 2009 averages, obtained from Remote Sensing Systems.